International Journal of Microwave and Wireless Technologies

cambridge.org/mrf

Accurate extraction method and analysis of the resonance parameters of a differential SRR-based RF sensor

Josephine Pichereau[1], Hakim Takhedmit[1], Ulrich Kuhl[2], Olivier Legrand[2], Jimmy Leszczynski[1], Stéphane Protat[1], Patrick Poulichet[1], Olivier Français[1] and Elodie Richalot[1]

[1]Université Gustave Eiffel, CNRS, ESYCOM, Marne-la-Vallée, France and [2]Université Côte d'Azur, CNRS, Institut de Physique de Nice (INPHYNI), Nice, France

Research Paper

Cite this article: Pichereau J, Takhedmit H, Kuhl U, Legrand O, Leszczynski J, Protat S, Poulichet P, Français O, Richalot E (2026) Accurate extraction method and analysis of the resonance parameters of a differential SRR-based RF sensor. *International Journal of Microwave and Wireless Technologies* **18**(3), 523–531. https://doi.org/10.1017/S1759078726103316

Received: 17 November 2025
Revised: 27 April 2026
Accepted: 30 April 2026
First published online: 17 June 2026

Keywords:
concentration sensor; dielectric characterization; differential measurement; equivalent circuit; liquid solutions; Lorentzian fitting; microwave sensor; parameter extraction; RF measurement; split ring resonator

Corresponding author: Josephine Pichereau; Email: josephine.pichereau@univ-eiffel.fr

Abstract

This paper presents a differential split-ring resonator sensor, designed for the analysis of small volumes around 20 µl of liquid. One resonator is filled with a reference liquid while the other contains the liquid under test. Although the differential configuration reduces the influence of environmental parameters, it can lead to resonance overlap when the dielectric properties of the two liquids are close to each other. To overcome this limitation, a post-processing method based on Lorentzian fitting is used to accurately extract resonance parameters such as frequency and width, even when the resonances strongly overlap. The method is validated through experiments with water–ethanol mixtures of different concentrations. This shows excellent agreement between measured and calculated values. Eigenmode simulations are also performed to analyze field distributions, providing additional insight into resonance behavior. The proposed approach offers a reliable and general methodology for the analysis of differential resonant sensors.

Introduction

Resonant RF-sensors have the advantage of greater sensitivity compared to broadband ones. However, their resonance properties are also sensitive to factors related to the measurement environment, such as temperature or physiological state, in the medical domain, food industries, and pharmaceutical fields [1–3]. This harms the extraction reliability of the parameters of interest if the measurement conditions are not well controlled. To overcome this problem, the design of specific RF-sensors providing indicators which are robust to measurement conditions is essential.

In this paper, split-ring resonators (SRRs) have been chosen because of their high quality factor, their compatibility with microfluidic systems, and their ability to analyze small samples [4, 5]. To avoid the aforementioned sensitivity to measurement conditions, a differential approach has been adopted. In parallel with the sample under test, another sample is used as a reference, and both samples are placed under the same conditions of temperature, humidity, etc. This allows increasing the reliability of the sensor [5–7] and improving the sensor sensitivity by reducing the response dependence on the above external parameters [6, 8, 9].

The resonance associated with the material under test is thus compared to the one related to the reference sample.

However, in some configurations, when both resonance frequencies are close to each other, an overlap of resonance peaks occurs making the extraction of resonance frequencies and bandwidths using classical approaches impossible. To distinguish the width as well as the resonance frequency of each peak, a fitting method with a sum of Lorentzian functions is proposed in this paper. This method has been used to investigate tunneling effects, i.e., very close resonances [10]; thus, it should be applicable for our RF-sensor. This post-processing method will be exposed, and its ability to extract the resonance parameters of the differential RF-sensor will be demonstrated.

In order to analyze the performance of the proposed sensor based on two SRRs excited by a microstrip line along with the post-processing technique, this paper presents measurement results obtained with a panel of water–ethanol solutions at different concentrations. The choice of these test samples is motivated by the range of applications linked to this type of analysis. The sensor geometry permits flexibility in the reference liquid choice; with water as reference,

© The Author(s), 2026. Published by Cambridge University Press in association with The European Microwave Association.

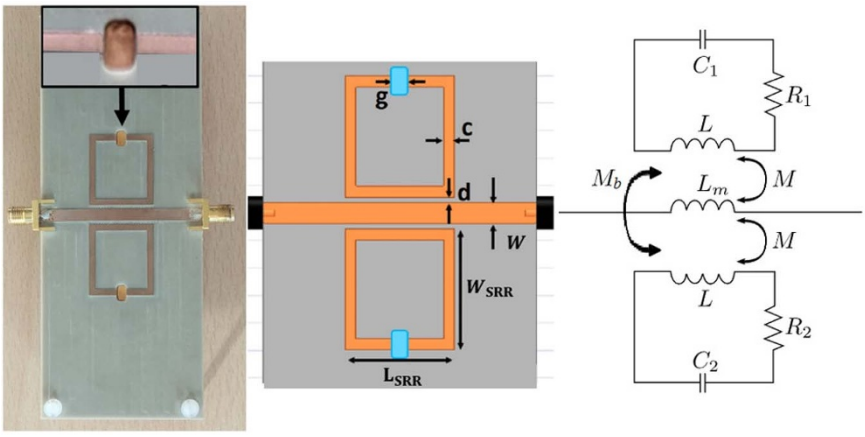


Figure 1. Presentation of sensor consisting of two SRRs excited by a microstrip line: Photograph of the fabricated sensor (left), a sketch indicating the geometrical parameters (middle), and an equivalent circuit model of the sensor consisting of two RLC-circuits (related to both SRRs) inductively coupled to the transmission line via M, with a mutual inductance between resonators M_b (right).

industrial applications concerning water sanitation [11] or biological analysis [12] can be targeted, as in [9] where a SRR-based differential microwave sensor is used with water as reference sample to monitor variations of electrolyte concentration in urine samples.

In order to discuss the extracted parameters in the different loading conditions, an in-depth analysis of the resonance modes properties is conducted. It highlights the coupling phenomena between both resonators and reveals symmetry properties of the field distribution that impact the coupling conditions between the resonators and the excitation line.

The main contribution of this paper is the modeling, design, and experiments of a differential SRR-based sensor combined with a Lorentzian post-processing method that enables accurate extraction of overlapping resonances. The proposed method offers improved stability and robustness against environmental variations compared to single-ended conventional SRR sensors.

An earlier version of this paper was presented at the 19th Conference of Antennas and Propagation (EuCAP 2025) and was published in its Proceedings [13].

Materials and methods

Sensor's presentation

The sensor (Fig. 1) consists of a microstrip line (operating in transmission mode) loaded symmetrically by two rectangular SRRs printed on a 1.524 *mm* thick Arlon 25N substrate ($\epsilon_r = 3.32$; $\tan\delta = 0.0025$) with 17 μm thick copper metallization. The width of the microstrip line W is dimensioned to have a 50 Ω characteristic impedance ($W = 3.8$ *mm*). The detection area of each SRR corresponds to the aperture of the metallic ring. In order to take advantage of the strong electric field amplitude within the substrate, the gaps in both resonators have been carved [14]. These cavities, having each one a small volume of around 23 μl per hole, can then be filled (using a syringe) with the liquids under test. The width of each SRR W_{Srr}, its length L_{Srr}, the distance between each SRR and the microstripline d, the gap g and the SRR line width c are, respectively, of 22 *mm*, 20 *mm*, 1 *mm*, 3 *mm*, and 2 *mm*. The unloaded resonant frequency is 1.35 GHz.

While modeling the rectangular SRR as a combination of an inductance, a resistor and a capacitor, the equivalent circuit representation of the differential sensor is shown in Fig. 1 (right) [6].

The access microstrip line is modeled by an inductance L_m, and both SRRs are coupled with the microstrip line through the mutual inductance M, whereas M_b represents the mutual coupling between both resonators. When both sensors are symmetrically loaded (using the same sample in both gaps), C_1 is equal to C_2 and R_1 is equal to R_2. When the material under test is placed in the gap of the SRR, the equivalent capacitance associated with the gap is modified, which subsequently leads to a shift in the resonant frequency [4]. Using two SRRs permits to achieve differential measurements when both SRRs are loaded asymmetrically. In particular, one SRR can be used as a reference if it is loaded by a sample of known properties. This differential approach reduces the impact of the environment on the measurement results [8].

Fabrication and methods for liquid mixing

The sensor (on the left of Fig. 1) has been fabricated in the ESYCOM laboratory using the LPKF Protomat S100 prototyping machine, based on mechanical etching. Water–ethanol solutions with different concentrations were produced in 50 *ml* flasks using 0.2 *ml* precision pipettes. To measure their dielectric properties, the commercial Keysight 85070E Dielectric Probe Kit [15] has been used, and the obtained values are compared here with the ones obtained using Birchak's theoretical mixing law [16, 17] over the frequency band from 1 GHz to 1.5 GHz. Birchak's law is used to define the parameters of the Debye model (Eq. 1) that are the low-frequency (Eq. 2) and the high-frequency (Eq. 3) permittivities of the different liquid mixtures according to the ratio α of a first liquid volume to the total bi-liquid mixture volume. The relaxation frequency (Eq. 4) is calculated following [18]. Thus, the frequency variation of the complex relative permittivity of each mixture is obtained.

$$\epsilon^*_{r(mix)} = \epsilon_{\infty(mix)} + \frac{(\epsilon_{s(mix)} - \epsilon_{\infty(mix)})}{1 + j\frac{f}{f_{rel(mix)}}} \tag{1}$$

$$\epsilon_{s(mix)} = \left[\alpha\sqrt{\epsilon_{s(1)}} + (1-\alpha)\sqrt{\epsilon_{s(2)}}\right]^2 \tag{2}$$

$$\epsilon_{\infty(mix)} = \left[\alpha\sqrt{\epsilon_{\infty(1)}} + (1-\alpha)\sqrt{\epsilon_{\infty(2)}}\right]^2 \tag{3}$$

$$f_{rel(mix)} = \exp\left[\alpha\ln(f_{rel(1)}) + (1-\alpha)\ln(f_{rel(2)})\right] . \tag{4}$$

https://doi.org/10.1017/S1759078726103316 Published online by Cambridge University Press

Table 1. Material parameters of the Debye model at 25°C

Material	ϵ_s	ϵ_∞	f_{rel} (GHz)
Water	78.36	5.2	19.24
Ethanol	24.43	4.5	0.96

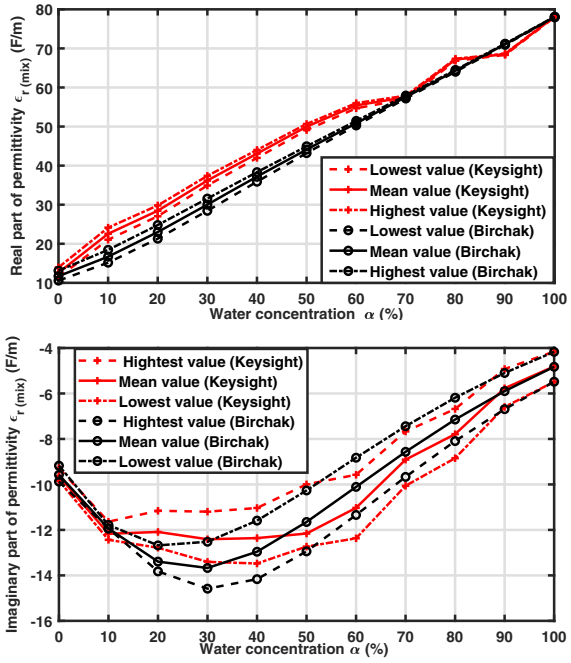


Figure 2. Real and imaginary parts of relative permittivities extracted by the Keysight probe compared to the ones given by the Birchak mixing law in the 1–1.5 GHz frequency band: mean, minimal, and maximal values over this frequency band for each water percentage of the mixtures.

Note that $\epsilon_{s(1)}$, $\epsilon_{\infty(1)}$, and $f_{rel(1)}$ are, respectively, associated with the low-frequency permittivity, high-frequency permittivity and relaxation frequency of the first liquid in the mixture, while $\epsilon_{s(2)}$, $\epsilon_{\infty(2)}$, and $f_{rel(2)}$ are related to the second liquid in the mixture. The frequency is denoted f. In our case, the two liquids of interest are water and ethanol, whose Debye's parameters are depicted in Table 1. Figure 2 depicts the mean, minimal, and maximal values, over the 1-1.5 GHz frequency band, of the permittivity's real and imaginary parts of the measured liquid samples that are obtained using Birchak's formulae and measured using the Keysight probe. The measured real part (polarization effect) is consistent with the mixing law, whereas the imaginary part (loss effect) follows the same pattern but with fluctuations around the expected values. Note that the imaginary part of the permittivity is negative due to the chosen time dependence as $e^{j\omega t}$. The various errors encountered can be associated with the uncertainties during the sample preparation process along with the Keysight probe resolution of $\pm 5\%$ for the real and imaginary parts [15].

Measurement and simulation post-processing method to extract the resonance parameters

Experimental conditions and measurement results

Transmission measurements between both SMA accesses are performed using a Rohde & Schwarz ZNB20 Vector Network Analyzer (VNA) with 2001 frequency points between 1 and 1.5 GHz. To carry out differential measurements, the cavity of one resonator is loaded with a reference sample that remains unchanged during the series of measurements, while the cavity of the second resonator is successively loaded with deionized water–ethanol solutions with different concentrations.

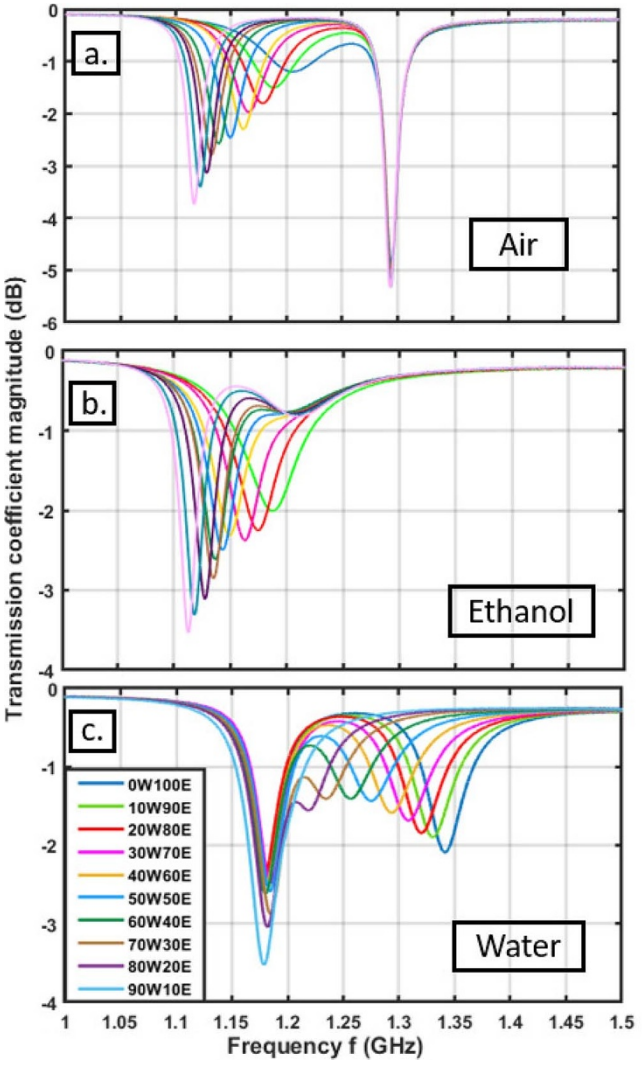


Figure 3. Measurement campaigns with different references were not carried out at the same time. Since the reproducibility of measurements with the sensor cannot be guaranteed, a frequency shift of the reference is possible from one measurement campaign to another, particularly because the sample volume is not controlled or monitored. Transmission coefficient magnitude for a reference sample of (a) air (top), (b) ethanol (middle), or (c) water (bottom) in one SRR, whereas the second SRR is loaded with a mixture of deionized water and ethanol of varying concentration, including the pure ethanol and water cases: legend "water mWnE" means water as reference, m% of water and n% of ethanol.

Three different reference choices have been considered: air (empty resonator), ethanol, and deionized water (Fig. 3). The measurement campaigns with the different references were not all carried out at the same time. Since the reproducibility of measurements with the sensor is not guaranteed, a frequency shift in the reference is possible from one measurement campaign to another, particularly because the sample volume is not controlled or monitored. However, this does not affect the resonance extraction method presented in this paper.

https://doi.org/10.1017/S1759078726103316 Published online by Cambridge University Press

Different behaviors are observed depending on the reference choice. With air as reference (Fig. 3a), two separated resonance peaks are observed for every mixture concentration, with a fixed resonance at 1.29 GHz corresponding to the reference (unloaded resonator), whereas the second resonance frequency decreases when the water concentration increases in agreement with the relative permittivity real part increase (Fig. 2). The highest difference between both resonance frequencies, obtained in the air/water loading case, is 174 MHz. When ethanol is used as a reference (Fig. 3b), two resonance peaks can still be distinguished when the second SRR is loaded with water; this loading case corresponds to the highest resonance frequency difference between both resonances, which is 98 MHz. This lower value in regard to the previous reference case (air) is explained by a smaller permittivity difference between both loading samples. When the ethanol concentration of the mixture increases, in particular for an ethanol concentration above 50%, it becomes difficult to distinguish both resonances due to a strong overlap between resonance peaks, so that there is no stable reference peak in this case. With the third reference choice (deionized water) (Fig. 3c), distinct resonance peaks are obtained for the lowest water concentrations of the mixtures, whereas resonance overlapping occurs when the mixture composition becomes closer to that of the reference sample.

In order to avoid this resonance overlap occurring in differential structures, some authors have proposed an asymmetric structure with a reference resonator associated with a resonance frequency outside the resonance frequency band of the sensing resonator [9]. In this paper, a symmetric structure has been chosen to permit the use of a reference liquid sample of the same type as the sample under test. Thus, the reference resonance is shifted in a very close way to the sample under test ensuring a weaker sensitivity to environmental effects than asymmetric sensors. The flexibility in the reference sample choice is an advantage of this differential structure as it can be adapted to the samples under test and the application objectives. The choice of a reference sample of permittivity far from the one of the sample under test permits a simple comparison of both resonance frequencies and widths, as both resonance peaks are separated; however, choosing a reference that fulfills this condition is difficult with samples of unknown properties. Besides, the choice of a reference sample similar to the sample under test can also be relevant for detecting a slight discrepancy between their compositions. As an example, a difference is observed in Fig. 3(c) between the transmission parameters measured with a mixture containing 90% of water and the one related to the very similar mixture containing 80% of water and 20% of ethanol, with a variation of the minimal transmission value, even though the two peaks are not distinguishable to the naked eye. In this case, the determination of the sensor resonance properties is not possible using classical resonance analysis techniques.

In the following analyses, the measurement results obtained with deionized water chosen as the reference material are depicted. Figure 3(c) depicts the magnitude variation of the measured transmission coefficients in the different asymmetrical loading conditions. One observes for all curves the presence of a magnitude peak around 1.18 GHz, which is related to the resonance of the SRR loaded by water, and a second resonance, also associated with a magnitude peak, whose position and width vary according to the mixture used. As expected, it is obvious that the highest difference between both resonance frequencies is obtained with the ethanol sample, whereas this difference decreases when the percentage of water within the mixture increases. The positions and widths of both peaks can be clearly distinguished as a function of mixture concentration in many cases. However, when the composition of both samples is close, as with the mixture composed of 90% of water and 10% of ethanol, the two resonances form a single peak so that it is difficult to distinguish their widths or central frequencies. This is why a post-processing method is proposed in the following; the complex value of the transmission coefficient will be exploited since the magnitude alone is not enough to extract the resonance properties.

Resonance parameters extraction method in resonance overlapping condition

The resonance of each SRR, associated with its RLC-equivalent model (on the right of Fig. 1), is modeled with an equation to a term having a frequency variation of the form:

$$S_r = \frac{A}{1 + j\,2\pi fRC - LC(2\pi f)^2} \tag{5}$$

with a numerator A slowly varying around the resonance frequency, leading to a resonance frequency of $f_r = \frac{1}{2\pi\sqrt{LC}}$ and a quality factor $Q = \frac{f_r}{\Gamma} = \frac{1}{2\pi f_r RC}$, where Γ is the resonance bandwidth [1]. As a consequence, the contribution of the SRR resonance to the transmission coefficient can be written as $S_r = (Af_r^2)/(f_r^2 - f^2 + jf\Gamma)$. Close to the resonance frequency, approximations can be performed ($f_r^2 - f^2 + jf\Gamma \approx 2f_r.(f_r - f) + jf_r\Gamma$) to simplify this expression and obtain the Lorentzian:

$$S_r = \frac{-A\frac{f_r}{2}}{f - (f_r + j\Gamma/2)}\,. \tag{6}$$

Therefore, to extract the properties of both resonances, even when their proximity induces an overlapping that makes them difficult to distinguish, the measured complex-valued transmission amplitude S_{21} is fitted by representing the two resonances as Lorentzians with a complex linear background:

$$S_{21} = \frac{a_1}{f - f_{r,1} - jf_{i,1}} + \frac{a_2}{f - f_{r,2} - jf_{i,2}} + c_1 f + c_0\,, \tag{7}$$

where a_i are the complex amplitudes, $f_{r,i}$ the eigenfrequencies, and $\Gamma_i = 2f_i$ the resonance widths ($i = 1, 2$). $c_1 \in \mathbb{C}$ are the slope of the linear background and $c_0 \in \mathbb{C}$ a constant. This fitting, however, requires first removing the frequency slope of the phase of S_{21} related to the propagation phenomenon along the microstrip line. This slope b is extracted from the measured argument, and the original transmission coefficient S_{21} is then modified through the multiplication:

$$\hat{S}_{21} = S_{21}\mathrm{e}^{-j(bf+\varphi_0)}\,, \tag{8}$$

where φ_0 is chosen to cancel out the phase outside the resonances. Figure 4 illustrates this operation, which consists of removing the global phase slope on the measurement results obtained with a mixture containing 80% of water and 20% of ethanol, as well as with a mixture of 90% of water and 10% of ethanol.

After this global phase slope removal, the transmission coefficient $\hat{S}_{ab}$ is fitted to the expression (7). As an example, Fig. 5 (respectively Fig. 4) shows the magnitude (resp. phase) of the measured transmission coefficient of a mixture composed of 80% of water and 20% of ethanol along with the fitting curve. To exemplify the modal overlapping effect, a very good agreement between the initial and fitted curves is observed (Inset Fig. 5 case 90% water and

https://doi.org/10.1017/S1759078726103316 Published online by Cambridge University Press

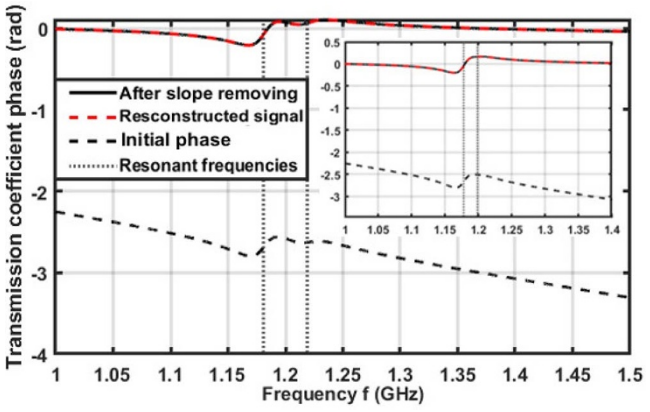


Figure 4. Measured phase of S_{21} with one SRR loaded by deionized water and the other one by a mixture of 80% water and 20% ethanol: initial values (in black), phase after removing the phase slope (as an initial step before performing the curve fitting), and fitted phase using the expansion on Lorentzians. Inset: the corresponding curves are presented for the 90W10E mixture.

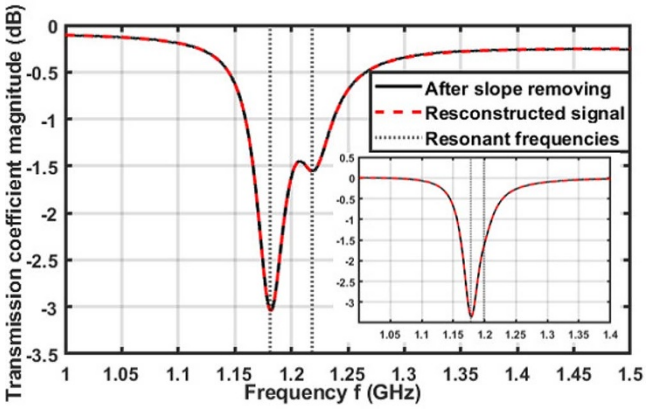


Figure 5. Initial and reconstructed transmission coefficient magnitude in the case of 80% water and 20% ethanol with water as reference. In the inset, the same curves are presented for the 90W10E mixture.

10% ethanol). The parameters extracted in this case using the fitting process are listed in Table 2 (for a frequency expressed in GHz in eq. (7)). Both resonance frequencies, at 1.181 and 1.219 GHz are indicated in Figs. 4 and 5. The dominant contribution of the first resonance, as indicated by a deeper peak in Fig. 5, results in a coefficient a_1 of magnitude 2.4 times higher than a_2. To amplify the modal overlapping effect, a mixture containing 90% of water and 10% of ethanol is presented in Figs. 5 and 4. In this case, the variation of the relative permittivities at 1.35 GHz between the reference sample (water) and the liquid under test (mixture with 90% of water) is of 7. The extracted parameters in Table 2 show the stability of the first resonance peak and a decrease of the second one, leading to a difference between both resonance frequencies of the same order of magnitude as the resonance widths. In spite of a strong modal overlap and an important imbalance between amplitudes, the agreement between initial and reconstructed curves is still excellent.

Extracted resonance parameters

The application of this presented fitting post-process has permitted the extraction of the resonance properties for all tested mixtures,

Table 2. Fitted parameters for two different water–ethanol mixtures with water as reference

Fitted parameter	80W20E	90W10E
$a_1/10^{-3}$	3.62+3.16j	-0.23 + 6.23j
$f_{r,1}$ (GHz)	1.18	1.18
$f_{i,1}$ (MHz)	17.4	18.9
$a_2/10^{-3}$	0.94+1.74j	-0.60 + 0.49j
$f_{r,2}$ (GHz)	1.22	1.20
$f_{i,2}$ (MHz)	18.5	15.8
c_0	1.01-0.48j	0.99 + 0.15j
c_1 (GHz^{-1})	-0.31-0.22j	0.01 - 0.12j

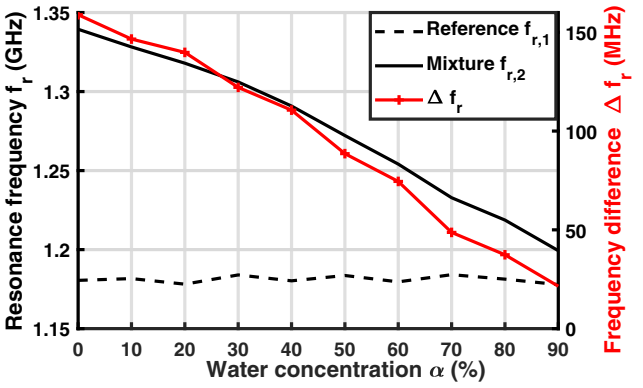


Figure 6. Variation of both extracted resonant frequencies, related to the reference material (water) and to the mixture, and difference between them. Values extracted from measured transmission coefficients through the curve fitting.

even in the case (90% of water, 10% of ethanol) where only one resonance peak is clearly visible in the transmission coefficient magnitude (Fig. 3). The variation of both resonance frequencies $f_{r,1}$ and $f_{r,2}$ is presented in Fig. 6 versus the water concentration of the tested mixture. The lowest resonance frequency $f_{r,1}$, mainly associated with the resonator loaded with water chosen as the reference when the resonances are well separated, remains stable, whereas $f_{r,2}$, associated with the liquid under test, decreases when the concentration of water increases. This is explained by the increase in the sample permittivity real part with water concentration (Fig. 2), which results in the increase of the capacitive effect C_2 and, as a consequence, in the decrease of the resonance frequency $f_{r,2} = 1/(2\pi\sqrt{LC_2})$. The difference between both resonance frequencies Δf_r is plotted in Fig. 6 (right vertical axis). This difference decreases almost linearly from 160 MHz to 20 MHz as the water concentration increases, in accordance with the real part of the mixture's permittivity. It becomes lower than the resonance width Γ_2 for a water concentration of 90% (Fig. 7), explaining the difficulty in distinguishing both resonances.

The resonance width Γ_1 associated with the reference is stable up to a water concentration of 50% and then increases as the resonances approach each other. The second resonance width Γ_2 varies similarly to the imaginary part of the mixture permittivity (Fig. 2) due to the losses induced by the sample, and can thus be used as an indicator of the material losses.

Table 3 presents a comparison of the proposed sensor with differential resonating sensors from the literature dedicated to small

https://doi.org/10.1017/S1759078726103316 Published online by Cambridge University Press

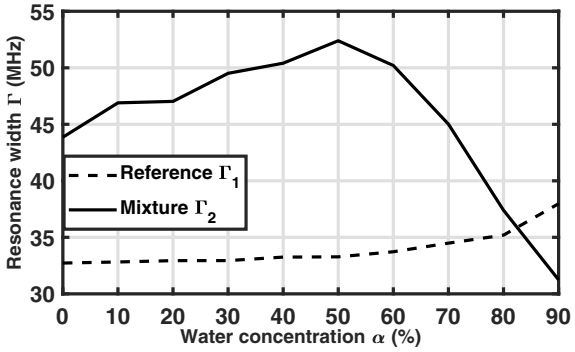


Figure 7. Resonance widths $\Gamma_1 = 2f_{i,1}$ and $\Gamma_2 = 2f_{i,2}$ as a function of the mixture water concentration.

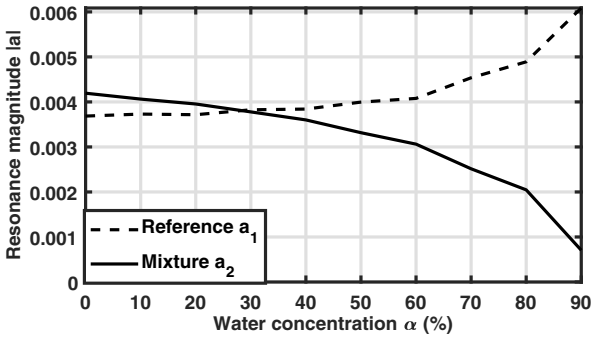


Figure 8. Magnitude of a_1 and a_2 coefficients as a function of the mixture water concentration.

Table 3. Comparative table of differential resonating sensors for liquid measurement

Ref	f_{empty} (GHz)	*Electrical size* ($10^{-4}\lambda_0^2$)	*S (%)*	*Extracted parameters*
[20]	1.618	7.27	0.626	$f_r\Gamma$
[21] sensor 1	6.69	5.17	0.11	f_r
[21] sensor 2	6.73	5.23	0.18	f_r
[21] sensor 3	6.81	5.35	0.09	f_r
[19]	4.15	5.28	0.11	f_r
[5]	0.97	12.5	0.91	$f_r\ min(\lvert S_{21}\rvert)$
Our sensor	**1.35**	**3.04**	**0.19**	$\mathbf{f_r\ \Gamma}$

liquid volume analysis. For a better comparison, the electrical size of the sensing surface is expressed as a function of the squared wavelength λ_0^2 corresponding to the empty resonator resonance frequency f_{empty}. The sensitivity is calculated for all sensors from the measurement of water–ethanol mixtures by averaging the relative sensitivities of the resonance frequency obtained with all the measured samples (of ethanol concentration varying from 0% to 100%). Air has been chosen as reference sample for this characterization. Our sensor exhibits an average relative sensitivity [19] $S = 0.19\%$ that is close to that of other differential resonating sensors of similar sensitive area. This table also highlights the extracted parameters. A major contribution of this paper lies in the presented post-processing approach that permits to extract both resonance frequencies and widths in all loading conditions, even in the case of strong overlap.

Due to the use of small liquid volumes, the impact of liquid evaporation as well as loading volume uncertainty on the extracted resonance frequencies has been evaluated through repeatability studies. Two loading conditions are considered with air as reference and water or ethanol as loading samples, and 25 successive measurements including the sample insertion step are carried out in each case. Whereas the highest resonance frequency (related to air) is very stable, with a normalized standard deviation of 2.3×10^{-5} with water and 3.0×10^{-4} with ethanol, higher variations are observed for the lowest resonance frequencies, with normalized standard deviations of 3.8×10^{-3} with water and 4.6×10^{-3} with ethanol.

In addition to resonance frequencies and widths, the extraction method also leads to the values of a_1 and a_2 coefficients whose modulus are presented in Fig. 8. Whereas similar magnitudes

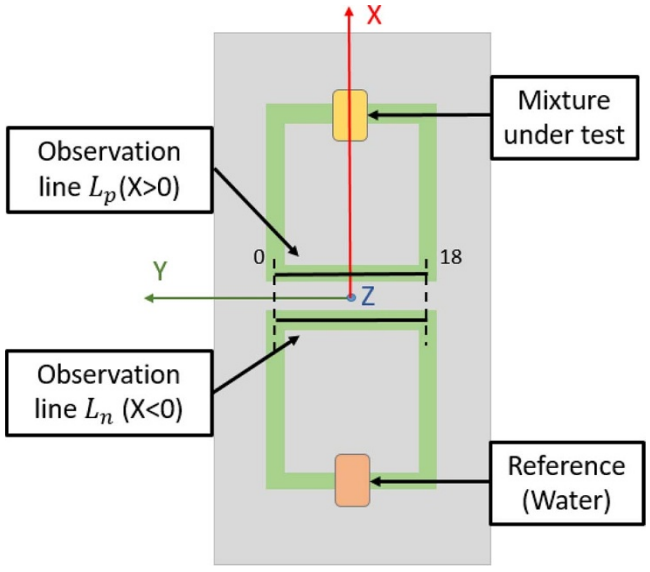


Figure 9. Simulated structure using eigenmode solver and definition of both observation lines for electric field distribution.

are obtained up to 50% of water, a discrepancy is then observed between both amplitudes, which complicates the extraction of the second resonance due to its lower amplitude. In particular, with 90% of water, the magnitude ratio between a_2 and a_1 is 0.11. In order to understand this imbalance in excitation of both resonance modes, their associated field distributions have been studied.

Resonance mode properties

In order to study the resonance mode properties, both coupled SRRs have been simulated without the excitation microstrip line using the eigenmode solver of Ansys HFSS software (Fig. 9). Liquid dielectric properties have been modeled using the Debye model along with mixing laws for the mixtures (Eqs. 1–4). For each loading condition, two eigenvalues (complex eigenfrequencies) and eigenvectors (electric field distributions) are determined. It should be noted that eigenvectors are known up to a multiplicative constant; the field distributions are presented here for a stored energy of 1 joule within the simulated volume. Moreover, due to leakages in the materials (substrate and liquids), a global phase choice has been made to obtain a globally minimized nonuniform imaginary part of the E_z component compared to its real part. The ensuing

https://doi.org/10.1017/S1759078726103316 Published online by Cambridge University Press

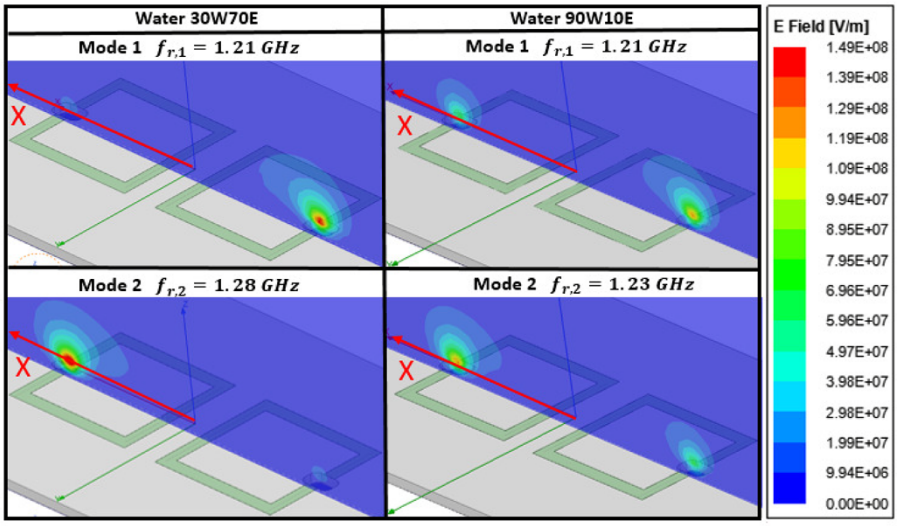


Figure 10. Electric field amplitude in the XOZ plane of both eigenmodes with an SRR (at $X > 0$) loaded with a water–ethanol mixture (30W70E or 90W10E) and the reference SRR (at $X < 0$) with deionized water.

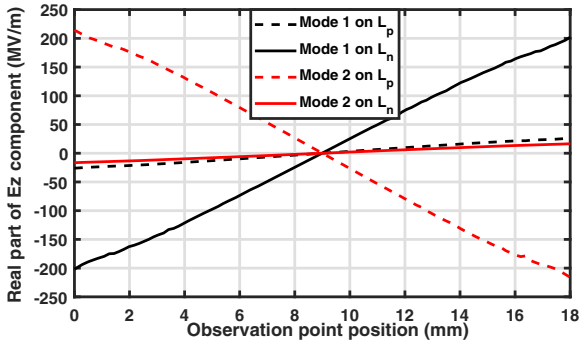


Figure 11. Real part of the E_z electric field component for both eigenmodes when an SRR (at $X > 0$) is loaded with the 30W70E mixture and the reference SRR (at $X < 0$) with deionized water. For each eigenmode, the electric field variation is observed on L_n and on L_p lines, respectively, on the resonator at X < 0 and at X > 0.

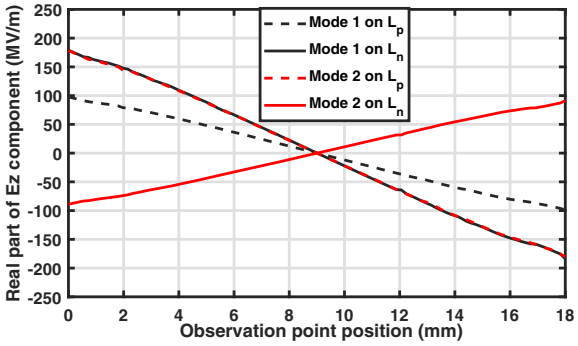


Figure 12. Real part of the E_z electric field component for both eigenmodes when an SRR (at $X > 0$) is loaded with the 90W10E mixture and the reference SRR (at $X < 0$) with deionized water. For each eigenmode, the electric field variation is observed on L_n and on L_p lines, respectively, on the resonator at X < 0 and at X > 0.

imaginary part being so small in all cases, we opted to present only the real parts in the following.

In order to highlight the field distribution differences between both resonators, two 18mm-long observation lines L_n and L_p parallel to the Y-axis are placed at the interface between the substrate and the resonators' metallic strips (Fig. 9); the position of both observation lines has been chosen for their proximity with the microstrip excitation line (not simulated here) to establish a link with the excited mode amplitudes shown in the previous section (Fig. 8). Simulations are performed with deionized water as the reference sample (cavity at $X < 0$) and different water–ethanol mixtures (cavity at $X > 0$). Two different cases of water–ethanol mixtures are studied, one with water concentration 30% and the other one with water concentration 90%. The eigenmode electric field amplitudes are presented in Fig. 10, whereas the real part of E_z component along both observation lines is presented in Fig. 11 with the 30W70E mixture and in Fig. 12 with the 90W10E mixture.

In each loading case, the resonance frequencies of both eigenmodes are indicated. A difference is observed with the values obtained when both resonators are excited by a microstrip line. For instance, the resonance frequency of the first mode is 1.21 GHz instead of 1.18 GHz obtained from the transmission coefficient (Table 2). This discrepancy is explained by the modification of the resonators' behavior and their mutual coupling due to the presence or absence of the microstrip line between them.

In all cases, the eigenmode of lower resonance frequency (mode 1) is associated with a higher electric field energy around the cavity loaded by the liquid having the highest permittivity real part which is water in this case (cavity at $X < 0$), whereas for mode 2 the electric field energy is higher around the cavity loaded by the mixture (cavity at $X > 0$). This is more marked when the dielectric properties of both samples are very different; for a mixture containing 30% of water, the energy is principally localized around one cavity (at $X < 0$ for mode 1 and at $X > 0$ for mode 2) (Fig. 10). The real part of E_z component is much higher along the observation line of the same resonator (that is L_n for mode 1 and L_p for mode 2) (Fig. 11). When the dielectric properties of both samples are closer (with a mixture containing 90% of water), the field amplitudes around both cavities (Fig. 10) as well as along both observation lines (Fig. 12) are more similar.

Additionally, it is of interest to observe the sign of E_z real part along L_n and L_p lines. For all loading conditions, the sign is the same on both observation lines for mode 1, whereas it is opposite for mode 2. As the E_z field component generated by a microstrip

https://doi.org/10.1017/S1759078726103316 Published online by Cambridge University Press

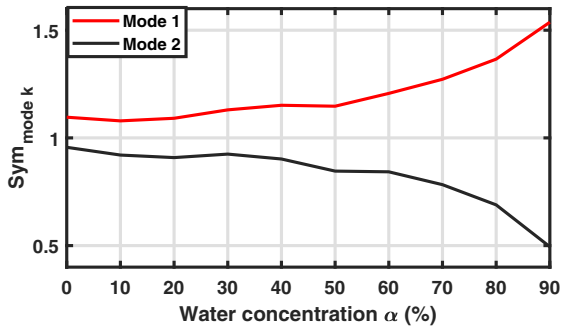


Figure 13. Symmetry indicator of both eigenmodes calculated according to Eq. 9 when deionized water is used as reference sample and mixtures of different water concentrations are inserted in the other resonator.

line is symmetric with respect to the YOZ plane, the excitation field better couples to mode 1 following the same symmetry. The impact of these mode symmetry properties remains weak when the field principally concentrates in one single resonator (as with 30W70E mixture), but the excitation of mode 2 becomes more difficult when the E_z real part on L_n is no longer negligible (as with 90W10E mixture). It explains why the amplitude of a_2 is 8 times smaller than a_1 with the 90W10E sample, whereas very close amplitudes are obtained with the 30W70E one (Fig. 8). The symmetry properties of both modes for every tested mixture are presented in Fig. 13 using the following symmetry indicator:

$$Sym_{mode\ k} = \frac{|E_{z,L_p,k,18mm} + E_{z,L_n,k,18mm}|}{max(|E_{z,L_p,k,18mm}|, |E_{z,L_n,k,18mm}|)}. \qquad (9)$$

calculated using the complex E_z field component at L_n and L_p right extremities (position 18mm) for each eigenmode k. The similar variation shape of this symmetry indicator with a_1 and a_2 amplitudes (Fig. 8) highlights the link between these symmetry properties and the excited mode amplitudes.

Conclusion

A resonating RF-sensor dedicated to the analysis of small liquid samples has been studied in this paper. In order to improve its robustness to environmental conditions that may vary in a given application context (as the physiological state of a patient or the temperature during an industrial process), a differential configuration is adopted, with one resonator loaded by a well-controlled liquid sample, whereas the liquid under test is placed in the second resonator. As experimentally shown, the presence of two cavities dedicated to the reference liquid and the liquid under test offers flexibility in the choice of the reference that can be done according to the aimed application and the tested sample properties. However, this measurement configuration requires the development of a post-processing method in order to precisely characterize both resonances even in the case of a strong overlap. The post-processing fitting method used in this paper, based on a representation of the resonances as Lorentzians, is shown to be well-suited in this context, with an excellent agreement between reconstructed and measured data; indeed, the resonance frequencies and widths along with the amplitudes of the resonance contributions have been extracted from a series of measurements using water–ethanol solutions with different concentrations, even when the dielectric properties of the mixture under test are close to the reference ones (chosen to be water). For a better understanding of the resonance mode properties as a function of their resonance frequency proximity, the resonance field distributions have been examined using eigenmode simulations, and different symmetry properties have been highlighted; this permits to explain the amplitude variation of both resonances with the liquid under test.

Regardless of the specific sensor configuration and studied liquid mixtures, the combination of a differential resonant sensor and Lorentzian-based post-processing offers a general and reliable method for the analysis of multi-resonant sensors. This approach, which allows to extract the complex resonance frequencies along with the resonance weights, can be extended to other frequency ranges, resonator geometries, and applications, paving the way toward more accurate and robust microwave sensors for the characterization of complex materials. We would like to emphasize that the proposed method can be applied whenever a small number of resonances contain the relevant information about the quantity of interest and the measured signal (preferably but not necessarily complex) is sufficiently dense in frequency to extract these resonances assuming a reasonably weak variation of the background and signal-to-noise ratio. Thus, it cannot only be applied to SRR sensors but also, for example, to MEMS-based sensors [22] and optical sensors [23].

Acknowledgements. The authors thank Thomas Legros for his help with repeatability measurements during his internship at the ESYCOM laboratory.

Competing interests. The author(s) declare none.

References

1. **Alahnomi RA, Zakaria Z, Ruslan E, Rashid SRA and Bahar AAM** (2017) High-q sensor based on symmetrical split ring resonator with spurlines for solids material detection. *IEEE Sensors Journal* **17**(9), 2766–2775.
2. **Galindo-Romera G, Herraiz-Martínez FJ, Gil M, Martínez-Martínez JJ and Segovia-Vargas D** (2016) Submersible printed split-ring resonator-based sensor for thin-film detection and permittivity characterization. *IEEE Sensors Journal* **16**(10), 3587–3596.
3. **Masini JD, Deshours F, Alquie G, Shahbaz R, Feruglio S, Meyer O, Galayko D, Kokabi H and Davaine J-M** (2025) Complementary split-ring resonator for non-invasive diagnosis of carotid artery atherosclerosis: Towards future in-vivo measurements. *IRBM* **46**(2), 100883, https://www.sciencedirect.com/science/article/pii/S1959031825000089
4. **Withayachumnankul W, Jaruwongrungsee K, Tuantranont A, Fumeaux C and Abbott D** (2013) Metamaterial-based microfluidic sensor for dielectric characterization. *Sensors and Actuators A: Physical* **189**, 233–237.
5. **Vélez P, Su L, Grenier K, Mata-Contreras J, Dubuc D and Martín F** (2017) Microwave microfluidic sensor based on a microstrip splitter/combiner configuration and split ring resonators (SRRs) for dielectric characterization of liquids. *IEEE Sensors Journal* **17**(20), 6589–6598.
6. **Ebrahimi A, Scott J and Ghorbani K** (2018) Differential sensors using microstrip lines loaded with two split-ring resonators. *IEEE Sensors Journal* **18**(14), 5786–5793.
7. **Xu L, Li F, Zhang S, Bai X, Wang Q and Chen J** (2025) Microwave sensor array based on differential mode detection strategy. *IEEE Microwave and Wireless Technology Letters* **35**, 257–260.
8. **Mohammadi S, Nadaraja AV, Luckasavitch K, Jain MC, Roberts DJ and Zarifi MH** (2020) A label-free, non-intrusive, and rapid monitoring of bacterial growth on solid medium using microwave biosensor. *IEEE Transactions on Biomedical Circuits and Systems* **14**(1), 2–11.
9. **Vélez P, Muñoz-Enano J, Grenier K, Mata-Contreras J, Dubuc D and Martín F** (2019) Split ring resonator-based microwave fluidic sensors

https://doi.org/10.1017/S1759078726103316 Published online by Cambridge University Press

for electrolyte concentration measurements. *IEEE Sensors Journal* **19**(7), 2562–2569.

10. **Gehler S, Löck S, Shinohara S, Bäcker A, Ketzmerick R, Kuhl U and Stöckmann H-J** (2015) Experimental observation of resonance-assisted tunneling. *Physical Review Letters* **115**, 104101.
11. **Harnsoongnoen S, Wanthong A, Charoen-In U and Siritaratiwat A** (2018) Planar microwave sensor for detection and discrimination of aqueous organic and inorganic solutions. *Sensors and Actuators B: Chemical* **271**, 300–305. https://www.sciencedirect.com/science/article/pii/S0925400518309791
12. **Juan CG, Potelon B, Quendo C and Bronchalo E** (2021) Microwave planar resonant solutions for glucose concentration sensing: A systematic review. *Applied Sciences* **11**(15), 7018. https://www.mdpi.com/2076-3417/11/15/7018
13. **Pichereau J, Takhedmit H, Kuhl U, Legrand O, Leszczynski J, Protat S, Poulichet P, Français O and Richalot E** (2025) Extraction and analysis of the resonance properties of a differential SRR-based RF sensor. In *2025 19th European Conference on Antennas and Propagation (EuCAP)*, pp. 1–5. 10.23919/EuCAP63536.2025.10999217
14. **Pichereau J, Fritiss Z, Takhedmit H, Poulichet P, Lanquetin L, Français O and Richalot E** (2023) Sensing biological materials with differential RF broadband and resonating microsensors. In *2023 IEEE Conference on Antenna Measurements and Applications (CAMA)*, pp. 65–70.
15. **Technologies A** (2013) High dielectric constant microwave probes forsensing soil moisture, agilent 85070e dielectric probe kit, p. 10, July 16 2013
16. **Birchak J, Gardner C, Hipp J and Victor J** (1974) High dielectric constant microwave probes for sensing soil moisture. *Proceedings of the IEEE* **62**(1), 93–98.
17. **Sihvola A** (2000) Mixing rules with complex dielectric coefficients. *Subsurface Sensing Technologies and Applications* **1**(4), 393–415.
18. **Yang L-J, Yang X-Q, Huang K-M, Shang H and Jia G-Z** (2010) Experimental and theoretic study of the dielectric properties of ethanol + methanol mixtures. *Journal of Solution Chemistry* **39**(4), 473–481.
19. **Liu W, Zhang J and Huang K** (2021) Dual-band microwave sensor based on planar rectangular cavity loaded with pairs of improved resonator for differential sensing applications. *IEEE Transactions on Instrumentation and Measurement* **70**, 1–8.
20. **Gan H-Y, Zhao W-S, Liu Q, Wang D-W, Dong L, Wang G and Yin W-Y** (2020) Differential microwave microfluidic sensor based on microstrip complementary split-ring resonator (MCSRR) structure. *IEEE Sensors Journal* **20**(11), 5876–5884.
21. **García V, Campos-Roca Y and García AG** (2024) Differential sensors in substrate integrated waveguide technology loaded with complementary split-ring resonators for liquid characterization. *IEEE Sensors Journal* **24**(1), 270–277.
22. **Zhao C, Montaseri MH, Wood GS, Pu SH, Seshia AA and Kraft M** (2016) A review on coupled mems resonators for sensing applications utilizing mode localization. *Sensors and Actuators A: Physical* **249**, 93–111. https://www.sciencedirect.com/science/article/pii/S0924424716303454
23. **Wang S, Pi H, Feng Y and Yan J** (2023) Optical mode localization sensing based on fiber-coupled ring resonators. *Opt. Express* **31**(13), 21 834–21 844. https://opg.optica.org/oe/abstract.cfm?URI=oe-31-13-21834

https://doi.org/10.1017/S1759078726103316 Published online by Cambridge University Press